Railway sleeper vibration measurement by train-borne laser Doppler vibrometer and its speed-dependent characteristics

Zeng, Y.; Núñez, A.; Li, Z.

DOI
10.1111/mice.13150

Publication date
2024

Document Version
Final published version

Published in
Computer-Aided Civil and Infrastructure Engineering

DOI: 10.1111/mice.13150

RESEARCH ARTICLE

COMPUTER-AIDED CIVIL AND INFRASTRUCTURE ENGINEERING WILEY

Railway sleeper vibration measurement by train-borne laser Doppler vibrometer and its speed-dependent characteristics

Y. Zeng | **A. Núñez** | **Z. Li**

Section of Railway Engineering, Faculty of Civil Engineering and Geosciences, Delft University of Technology, Delft, The Netherlands

Correspondence
A. Núñez, Faculty of Civil Engineering and Geosciences, Delft University of Technology, Stevinweg 1, Delft, The Netherlands.
Email: A.A.NunezVicencio@tudelft.nl

Funding information
ProRail and the Project Reliable Embankments for Safe Expansion in Rail Traffic (RESET)

Abstract

A train-borne laser Doppler vibrometer (LDV) directly measures the dynamic response of railway track components from a moving train, which has the potential to complement existing train-borne technologies for railway track monitoring. This paper proposes a holistic methodology to characterize train-borne LDV measurements by combining computer-aided approaches and real-life measurements. The focus is on the speed-dependent characteristics because the train speed affects the intensity of railway sleeper vibrations and the intensity of speckle noise, which further affects the quality and usability of the measured signals. First, numerical models are established and validated to simulate sleeper vibrations and speckle noise separately. Then, a vibration–noise separation method is proposed to effectively extract speckle noise and structural vibrations from LDV signals measured at different speeds. The parameters of the separation method are tuned using simulation signals. The method is then validated using laboratory measurements in a vehicle-track test rig and applied to field measurements on a railway track in Rotterdam, the Netherlands. Further, the speed-dependent characteristics of train-borne LDV measurement are determined by analyzing the competition between sleeper vibrations and speckle noise at different speeds. Simulation and measurement results show that an optimal speed range yields the highest signal-to-noise ratio, which varies for different track structures, measurement configurations, and operational conditions. The findings demonstrate the potential of train-borne LDV for large-scale rail infrastructure monitoring.

1 | INTRODUCTION

The dynamic properties of railway track structures can affect the load-bearing capacity of rail infrastructure, the interaction between trains and tracks, and the safety of operations. Due to train load and aging, track dynamic properties degrade over time and deviate over different locations. Thus, monitoring these properties for well-informed, effective, and efficient track maintenance is essential (Wang et al., 2016). Since a running train is a natural source to excite the dynamic response of railway tracks over a broad frequency band, vibration measurement under operational conditions is a preferred approach to assess the dynamic properties of railway tracks.

Existing vibration-based techniques for monitoring railway track dynamic properties can be divided into trackside and train-borne vibration measurements. In the former category, sensors are usually mounted on rails (Yue et al., 2016), sleepers (Le Pen et al., 2016), ballast (Liu et al., 2021), or concrete slabs (Zhang et al., 2021) to measure their dynamic response under train passage and to support the identification of track properties. However, these techniques are cost-prohibitive for large-scale infrastructure monitoring, so they are usually applied at hot spots, such as joints (Yang et al., 2018) and crossings (Boogaard et al., 2018; Shen et al., 2019). In the category of train-borne measurements, sensors are mounted on trains, such as on their axle boxes or bogie frames, to detect anomalies in railway tracks (Bocciolone et al., 2007; Li et al., 2022; Salvador et al., 2016). These techniques are effective in detecting anomalies on rails, such as rail surface defects (Li et al., 2015; Li & Shi, 2019), degraded joints (Molodova et al., 2016), poor-quality welds (Molodova et al., 2008), and degraded crossings (Wei et al., 2017). In recent years, methods have been developed to utilize train vibrations to monitor track layers below rails, such as hanging sleepers and mud-pumping locations (Berggren et al., 2014; Sresakoolchai & Kaewunruen, 2022).

A laser Doppler vibrometer (LDV) is a noncontact sensing instrument that measures vibration velocity by utilizing Doppler frequency shift. It can provide high accuracy and sensitivity for vibration measurements over a wide range of frequencies (Lutzmann et al., 2011). LDV has been widely applied to engineering structures for modal analysis and damage detection (Lutzmann et al., 2011; Rothberg et al., 2017), while in most applications, the laser spot measures at discrete points (Muramatsu et al., 2020; Siringoringo & Fujino, 2009) or along a closed path (Chen et al., 2018; Di Maio et al., 2021). A train-borne LDV can target its laser spot on tracks and directly measure track vibrations in response to the moving train. In simulation studies, train-borne LDVs are used to identify bridge mode shapes (OBrien & Malekjafarian, 2016) and estimate transfer functions of track structures (Zeng, Núñez, et al., 2023). In experimental studies, train-borne LDVs measure rail vibrations to identify rail bending modes (Kaynardag et al., 2021) and detect welds (Kaynardag et al., 2023).

Many existing technologies rely on train vibrations to indirectly sense track behaviors, which is challenging for monitoring track layers below rails since their responses decay and mix with those of other train-track components as they are transmitted to sensors on trains. In contrast, a train-borne LDV can directly measure the vibration of track layers below rails, for example, railway sleepers. Train-borne LDV is not in a position to compete with existing technologies but to provide purer information about the dynamic behavior of track structures, thus enabling more effective rail infrastructure monitoring. However, train-borne LDV is still a fairly new technology with limited field testing. To fill the gaps for large-scale applications, more analysis is needed. A major factor of concern is train speed, which can affect train-borne LDV measurements in two aspects.

(1) *Influence of train speeds on track dynamics*. Track vibrations are excited by wheel-rail contact forces, including quasi-static components due to moving loads and dynamic components due to track irregularities (Milne et al., 2017). As the train speed increases, wheel passage and sleeper passage frequencies increase linearly, and the corresponding track response first increases and then may decrease after resonance (Auersch, 2006; Le Pen et al., 2016; Yue et al., 2017). For the dynamic response due to irregularities, its frequencies increase linearly with the increasing train speed, while the track vibration amplitude increases first fast and then slowly (Bian et al., 2015). Therefore, the dependency of track vibrations on train speeds is affected by several different mechanisms simultaneously, leading to a complex nonlinear behavior. In addition, a train-borne LDV measures a track component only when the laser spot scans its surface. As the train speed increases, the signal length becomes shorter, which may lead to more uncertainties in the measured response.
(2) *Influence of train speeds on speckle noise*. Speckle noise originates from speckle patterns that appear when a laser beam is scattered from an optically rough surface (Martin & Rothberg, 2009). Speckle noise appears as irregular and random spikes or dropouts in an LDV signal and as a broadband noise floor in its spectrum (Rothberg et al., 2017). The severity of speckle noise depends on the properties of the laser and the target surface as well as the change of speckle patterns due to the in-plane motion of the laser spot on the target surface (Rothberg et al., 2017). The speed of such in-plane motion is reported to be the most influential factor in speckle noise behavior (Martarelli & Ewins, 2006). Simulations and experiments show that the amplitude of speckle noise increases with the increase in in-plane speeds (Jin et al., 2022; Rahimi et al., 2014; Sracic & Allen, 2009). In most LDV applications, speckle noise is mitigated through discrete-point measurements (Revel et al., 2011; Sels et al., 2019), repeated closed-path scanning (Allen & Sracic, 2010; Stanbridge et al., 2004), or surface treatment (Xu et al., 2017). However, these solutions are incompatible with train-borne LDV that scans the surface of railway tracks along an open path. Many conventional filtering methods have been tried to handle speckle noise, for example, median filter (Arruda et al., 1996), low-pass filter (Stanbridge et al., 2004), and wavelet denoising (Katicha

et al., 2014). However, their performance has been found unsatisfactory (Jin et al., 2022; Stanbridge et al., 2004).

Therefore, specialized signal processing methods are needed to reduce speckle noise in LDV signals. Several methods have been developed for measurements at small in-plane speeds (0–0.1 m/s), in which speckle noise is detected and replaced through interpolation or prediction (Aranchuk et al., 2006; Lv et al., 2019; Wang et al., 2021). Recently, a few methods have been developed to mitigate speckle noise at higher in-plane speeds. Low-pass filtering and oscillation detrending are combined, and it is tested at different speeds (0.1 m/s, 10 m/s, 20 m/s) for a case of harmonic vibrations (Jin & Li, 2022). An ensemble empirical mode decomposition method is proposed and validated at fixed speeds (0.85 m/s and 10 km/h) in two experimental cases (Jin et al., 2022). However, selecting parameters, such as the number of intrinsic mode functions, requires human judgment and can vary for different experiments and speeds. A three-step speckle noise reduction framework is proposed and validated at different speeds (0.5 km/h, 5 km/h, 20 km/h), in which different parameters are used for different speeds (Zeng et al., 2022). There is still a lack of effective methods to reduce speckle noise adaptively for LDV signals measured at different speeds.

The variation of track vibration and speckle noise with respect to train speed affects the quality and usability of train-borne LDV signals. To the best of our knowledge, no published research has investigated the speed-dependent characteristics of a train-borne LDV for track vibration measurements. In this context, the main contributions of this paper are given as follows.

(1) This paper presents the world's first field test of a train-borne LDV for measuring railway sleepers on an operational railway line. The effective extraction of the sleeper vibration demonstrates the applicability of the technology to large-scale monitoring of railway tracks under operational conditions.
(2) A holistic methodology combining computer-aided approaches and real-life measurements is proposed to characterize train-borne LDV measurements and determine the speed-dependent characteristics of their signal-to-noise ratio (SNR). Numerical models are used to simulate the sleeper vibration and speckle noise separately. Laboratory and field measurements further test the train-borne LDV technology under well-controlled and real-field conditions, respectively.
(3) A specialized method is developed to separate speckle noise from structural vibrations in LDV signals measured at different speeds. The parameters are tuned with simulated signals, and the performance is verified with laboratory measurements. The separation method using the same parameters works robustly under different scenarios.

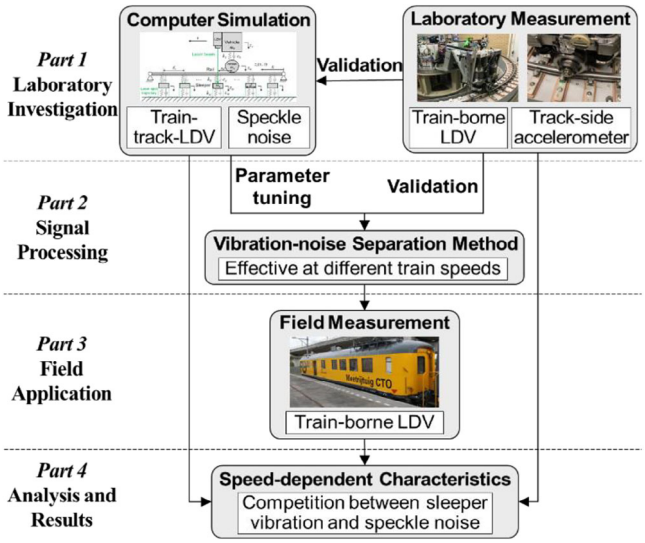

FIGURE 1 Methodology for characterizing train-borne laser Doppler vibrometer (LDV).

Figure 1 illustrates the methodology of this research. In Part 1, numerical models of train-track-LDV dynamics and speckle noise are established and validated with laboratory measurements. This provides insights into the train-borne LDV system prior to field tests and enables sleeper vibrations and speckle noise to be characterized separately without interfering with each other. Since structural vibration and speckle noise are mixed in real-life measurements, Part 2 presents a signal processing method to separate them effectively at different train speeds. The parameters of the separation method are tuned using simulation signals, and the method is then validated with laboratory measurements under well-controlled and well-observed conditions. In Part 3, field measurements of sleeper vibration using a train-borne LDV are performed in Rotterdam, the Netherlands, and the validated separation method is applied to the measured signals. In Part 4, the speed-dependent characteristics are investigated based on the simulations, laboratory, and field measurements. Sections 2–5 of this paper present Parts 1–4, respectively, and conclusions are drawn at the end.

2 | SIMULATION AND VALIDATION

2.1 | Numerical modeling

This research first uses modeling and simulation to characterize train-borne LDV measurement and generate signals

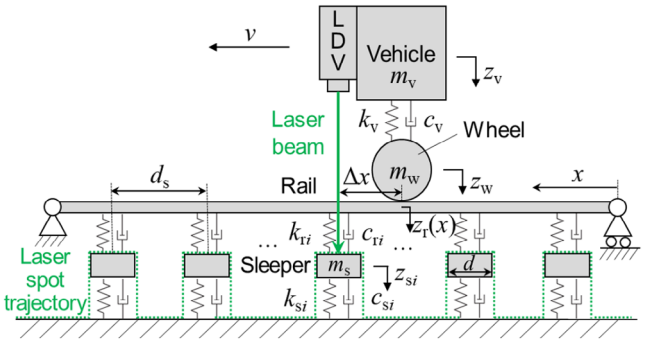

FIGURE 2 A train-track laser Doppler vibrometer (LDV) model.

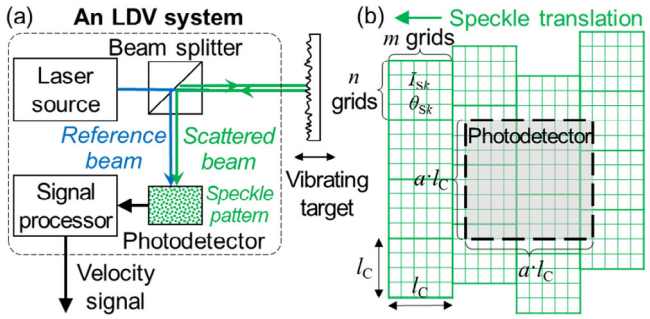

FIGURE 3 (a) Working principle of a laser Doppler vibrometer (LDV) measuring an optically rough surface. (b) Simulation of speckle translation.

of sleeper vibration and speckle noise. A vertical train-track model is built to simulate sleeper vibration measurement using a train-borne LDV (Zeng, Núñez, et al., 2023), as shown in Figure 2. The train is modeled as a quarter vehicle as follows,

$$m_v \ddot{z}_v(t) + k_v [z_v(t) - z_w(t)] + c_v [\dot{z}_v(t) - \dot{z}_w(t)] = 0 \quad (1)$$

$$m_w \ddot{z}_w - k_v [z_v(t) - z_w(t)] - c_v [\dot{z}_v(t) - \dot{z}_w(t)] + F_c(t) = 0 \quad (2)$$

where m_v and m_w are the masses of the vehicle and the wheel, respectively, z_v and z_w are their vertical displacements, respectively, k_v and c_v are the stiffness and damping of the suspension, respectively, and F_c is the wheel-rail contact force.

The track consists of a rail discretely supported by n_s rigid sleepers on a fixed foundation. The equation of motion of the i-th sleeper is:

$$m_s \ddot{z}_{si}(t) - k_{ri} [z_r(x_{si}, t) - z_{si}(t)] - c_{ri} [\dot{z}_r(x_{si}, t) - \dot{z}_{si}(t)] + k_{si} z_{si}(t) + c_{si} \dot{z}_{si}(t) = 0 \quad (3)$$

where m_s is the mass of the sleeper, z_{si} is its vertical displacement, k_{ri} and c_{ri} are the stiffness and damping of the rail pad above the i-th sleeper, respectively, k_{si} and c_{si} are the stiffness and damping of the ballast below the i-th sleeper, respectively, $z_r(x_{si}, t)$ is the vertical displacement of the rail at the position of the i-th sleeper, that is, $x_{si} = (i-1/2)d_s$ with d_s denoting the sleeper spacing.

The rail is represented by a simply supported Euler–Bernoulli beam, and its displacement at position x and time t is characterized by (Zhai, 2020),

$$EI \frac{\partial^4 z_r(x,t)}{\partial x^4} + m_r \frac{\partial^2 z_r(x,t)}{\partial t^2} = F_c(t)\delta(x - x_c(t)) - \sum_{i=1}^{n_s} k_{ri} [z_r(x_{si}, t) - z_{si}(t)] \delta(x - x_{si})$$

$$- \sum_{i=1}^{n_s} c_{ri} [\dot{z}_r(x_{si}, t) - \dot{z}_{si}(t)] \delta(x - x_{si}) \quad (4)$$

where E and I are the elastic modulus and second area moment of the rail, respectively, m_r is the mass per unit length of the rail, $\delta(\cdot)$ is the Dirac impulse function, x_c is the position of the wheel running along the track, that is, $x_c(t) = x_0 + vt$ with v denoting the train speed and x_0 denoting the initial position.

Hertz's theory is employed to calculate the wheel-rail contact force as follows (Zhai, 2020),

$$F_c(t) = \begin{cases} 0 & \text{when} z_w(t) - z_r(x_c, t) - z_e(x_c) < 0 \\ \left(\frac{1}{G}[z_w(t) - z_r(x_c, t) - z_e(x_c)]\right)^{3/2} & \text{otherwise} \end{cases} \quad (5)$$

where the contact coefficient G is $4.57 \times r_w^{-0.149} \times 10^{-8}$ m/N$^{2/3}$ with r_w denoting the wheel radius, and z_e is the rail irregularity.

Equation (4) is converted to second-order ordinary differential equations according to the Ritz method (Zhai, 2020), as presented in Appendix A. Then, they are solved together with Equations (1)–(3) numerically using the Newmark-β method (Newmark, 1959), while the contact force is updated at each time step according to Equation (5).

In Figure 2, an LDV is rigidly connected to the vehicle with its laser spot targeted onto the sleepers. The laser spot has an offset Δx from the wheel-rail contact point. Assuming that the vibration of the LDV can be perfectly removed from the LDV signal (Rothberg & Tirabassi, 2012), the vibration of the i-th sleeper is measured when the laser spot is on top of it, as expressed below.

$$\dot{z}(t) = \dot{z}_{si}(t) \text{when } x_{si} - \frac{d}{2} < vt + \Delta x < x_{si} + \frac{d}{2} \quad (6)$$

where d is the sleeper width.

Figure 3a shows the working principle of an LDV. A laser beam is projected onto a target surface, and the

scattered beam is collected on a photodetector. Due to the roughness of the target surface, the scattered light consists of coherent waves that interfere with each other, forming speckle patterns on the photodetector (Rothberg & Halkon, 2004). This phenomenon is inevitable since the surfaces of railway components are optically rough. Each speckle is then heterodyned with an additional reference beam, and the intensity is converted to a signal with the following frequency (Martarelli, 2001).

$$\omega_{\mathrm{D}}(t) = \omega_{\mathrm{R}} + \frac{4\pi}{\lambda}\dot{z}(t) + \frac{d\theta_{\mathrm{M}}}{dt}(t) \tag{7}$$

where ω_{R} is an artificial frequency shift, λ is the wavelength of the laser, $\dot{z}(t)$ is the vibration velocity of the target, and θ_{M} is a phase angle expressed as follows:

$$\theta_{\mathrm{M}} = \arctan\left[\frac{\sum_{k=1}^{K} a_k \sqrt{I_{Sk}} \sin(\theta_{\mathrm{R}} - \theta_{Sk})}{\sum_{k=1}^{K} a_k \sqrt{I_{Sk}} \cos(\theta_{\mathrm{R}} - \theta_{Sk})}\right] \tag{8}$$

where K is the total number of speckles, a_k is the area of the k-th speckle on the photodetector, I_{Sk} and θ_{Sk} are the intensity and phase of the k-th speckle, respectively, and θ_{R} is the phase of the reference beam. According to Equation (7), the speckle noise caused by the phase change rate $d\theta_{\mathrm{M}}/dt$ when measuring the target vibration $\dot{z}(t)$ is expressed as follows:

$$\xi(t) = \frac{\lambda}{4\pi} \cdot \frac{d\theta_{\mathrm{M}}}{dt}(t) \tag{9}$$

For train-borne LDV measurements, speckle translation due to the in-plane motion between the laser spot and the target surface plays a dominant role in $d\theta_{\mathrm{M}}/dt$ (Martin & Rothberg, 2009). The space and time correlation lengths of the speckles, l_{C} and τ_{C}, are two important parameters depending on the laser properties and measurement setup (Asakura & Takai, 1981). The space correlation length l_{C} characterizes the size of each speckle, within which I_{Sk} and θ_{Sk} are constants following a negative exponential distribution and a uniform distribution, respectively (Denman et al., 1996). The time correlation length τ_{C} describes the time length for the speckle pattern to advance by one speckle, which is inversely proportional to the in-plane speed v (Asakura & Takai, 1981). More details of the model can be found in Appendix B.

As shown in Figure 3b, each speckle is modeled as a square with $m \times n$ grids (Rothberg, 2006). A full speckle transition is divided into m partial transitions, and different columns are randomly misaligned along the n grids to account for speckle irregularities. The photodetector is of size $a \cdot l_{\mathrm{C}} \times a \cdot l_{\mathrm{C}}$, and the intensity and phase of the reference beam on the photodetector, I_{R} and θ_{R}, are assumed constant (Rothberg, 2006). In the simulation of speckle translation, the photodetector starts from an initial position and moves at the constant speed of $l_{\mathrm{C}}/\tau_{\mathrm{C}}$. At each partial transition, indexed by the j-th step, the overlapping area between the photodetector and each speckle is obtained, and the phase $\theta_{\mathrm{M}}(j)$ is calculated according to Equation (8). Then, the phase change rate at the j-th step is estimated as follows:

$$\frac{d\theta_{\mathrm{M}}}{dt}(j) = \frac{\Delta\theta_{\mathrm{M}}(j)}{\Delta t} = \frac{\theta_{\mathrm{M}}(j) - \theta_{\mathrm{M}}(j-1)}{(\tau_{\mathrm{C}}/m)} \tag{10}$$

where $\Delta\theta_{\mathrm{M}}$ should be constrained to be less than $\pi/2$.

Based on the simulated phase change rates, the speckle noise $\xi(t)$ is obtained according to Equation (9). A low-pass finite impulse response filter with cut-off frequency f_{C} is applied to $\xi(t)$ to resemble the signal acquisition process.

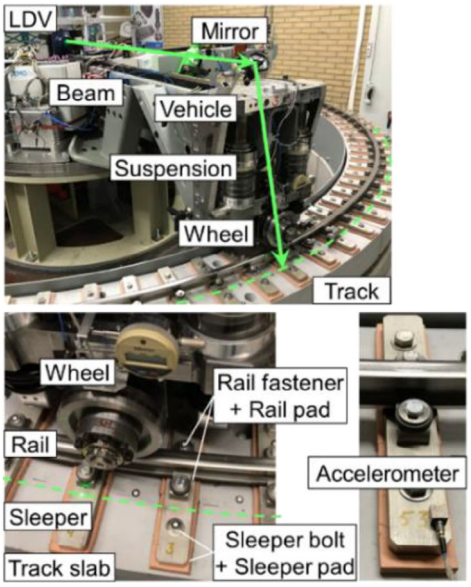

FIGURE 4 V-Track test rig instrumented with a laser Doppler vibrometer (LDV).

2.2 | Laboratory measurement

Laboratory measurements play an important role in this research to validate the numerical models and the signal processing method under well-controlled and well-observed conditions. They are performed in the vehicle-track test rig of TU Delft named V-Track (Naeimi et al., 2018), as shown in Figure 4. The scaled track structure is composed of rails, sleepers, and track slabs. Rails are supported by sleepers through fasteners and rail pads, and sleepers are assembled on track slabs through bolts and sleeper pads. A wheel running along the rail is loaded by suspensions. On top of the suspension, a vehicle is connected to a beam mounted with a Polytec RSV-150 LDV. Its laser beam is reflected onto the sleepers by a mirror fixed

on the end of the beam. As the beam rotates, the vehicle moves forward, the wheel rolls along the track, and the LDV scans the track surface. This enables the sleeper vibration to be excited by the wheel and then measured by the train-borne LDV. At the same time, the angular position of the beam is measured, which can be used to determine the position of the wheel and the laser spot. Moreover, PCB 356B21 accelerometers are installed on some sleepers to measure their vertical accelerations in response to the passing vehicle. An additional accelerometer is installed on the mirror to capture its effect on the LDV signal.

2.3 | Model validation

Table A1 lists the parameters for simulating the vehicle-track dynamics. The vertical irregularity of the rail z_e is generated by applying a low-pass Butterworth infinite impulse response filter to Gaussian white noise (Zeng, Núñez, et al., 2023). Such an artificial spectrum is defined by a passband wavelength λ_{pass}, a stopband wavelength λ_{stop}, and a stopband attenuation h_{stop}, and it is smoothly monotonic and maximally flat in the passband. It resembles the decay pattern of real-life track irregularity spectrum and enables the wheel-rail interaction to cover a wide range of frequencies.

The track dynamics model is validated using the trackside accelerometer measurements in V-Track. Figure 5a,b show the vibrations of the center sleeper simulated at two different vehicle speeds, respectively. The trackside measurements are compared with the simulation results after conversion from acceleration to velocity through frequency-domain integration (Brandt & Brincker, 2014). It can be seen that the amplitude and frequency of the sleeper vibration are larger at a higher speed. The simulation results are similar to the measurements in both time and frequency domains, but their amplitudes do not exactly match, especially at the higher speed, mainly due to the simplification of the model and the rail irregularity. Despite such differences, the model is considered suitable for simulating rigid-body vibrations of sleepers in a multilayer track structure under a moving train load. The model is fast to solve numerically, and its parameters are easy to tune due to the limited number. Using a more complex train-track model or more complex rail irregularity spectrum may yield a better match between simulations and the measurements. However, this requires additional efforts in modeling, parameter tuning, and computation. In cases of selecting from models of different complexity, a comparative analysis of their performance and effectiveness for the specific application may be necessary.

The speckle translation model is validated using speckle noise separated from LDV signals in laboratory measurements (the separation method will be introduced in Section 3). The simulation parameters are listed in Table B1, and the simulated speckle noise at two vehicle speeds is compared with the measurements in Figure 5c,d. It can be seen that, at a higher speed, spikes appear more frequently with greater amplitudes and shorter durations. The simulated speckle noise behaves similarly to the measurements in terms of the interval, amplitude, and duration of spikes. Meanwhile, good consistency can be observed over a wide frequency range. The simulated and measured speckle noise at the two speeds exhibit an average deviation of 8.4% in their standard deviations in the time domain and an average deviation of 10.6% in their means in the frequency domain (0–10 kHz). It should be noted that the simulation cannot exactly replicate the measurement due to the randomness of speckle patterns. Instead, the statistical agreement between them demonstrates the effectiveness of the model in reproducing the speckle noise.

3 | VIBRATION–NOISE SEPARATION

3.1 | A signal processing method

In real-life measurements, structural vibration and speckle noise are mixed. Thus, effective signal processing is needed to separate them. As introduced in Section 1, no existing method can achieve this adaptively at different speeds. In recent research (Zeng et al., 2022), spikes are first distinguished through a wavelet-based detection method. Then, the detected spikes are replaced with estimates through an autoregressive integrated moving average (ARIMA)-based imputation method. Finally, the residual noise is filtered out using a band-pass filter. However, the selected parameters of this method vary at different speeds due to the speed-dependent characteristics of spikes. To address this problem, the method is adapted to extract speckle noise and target vibration without the need to adjust its parameters for different speeds.

Step 1. Perform one-level discrete Haar wavelet decomposition and reconstruction (Amezquita-Sanchez & Adeli, 2016; Karim & Adeli, 2002) to a raw LDV signal $x_0(t)$ and calculate spike indicators $R_d(t)$ as follows:

$$cD_1(t) = \mathrm{DWT_D}\left[x_0(t)\right] \tag{11}$$

$$R_d(t) = \left|\mathrm{IDWT_D}\left[cD_1(t)\right]\right| \tag{12}$$

where $\mathrm{DWT_D}[\cdot]$ and $\mathrm{IDWT_D}[\cdot]$ represent forward and inverse discrete wavelet transforms, respectively, and

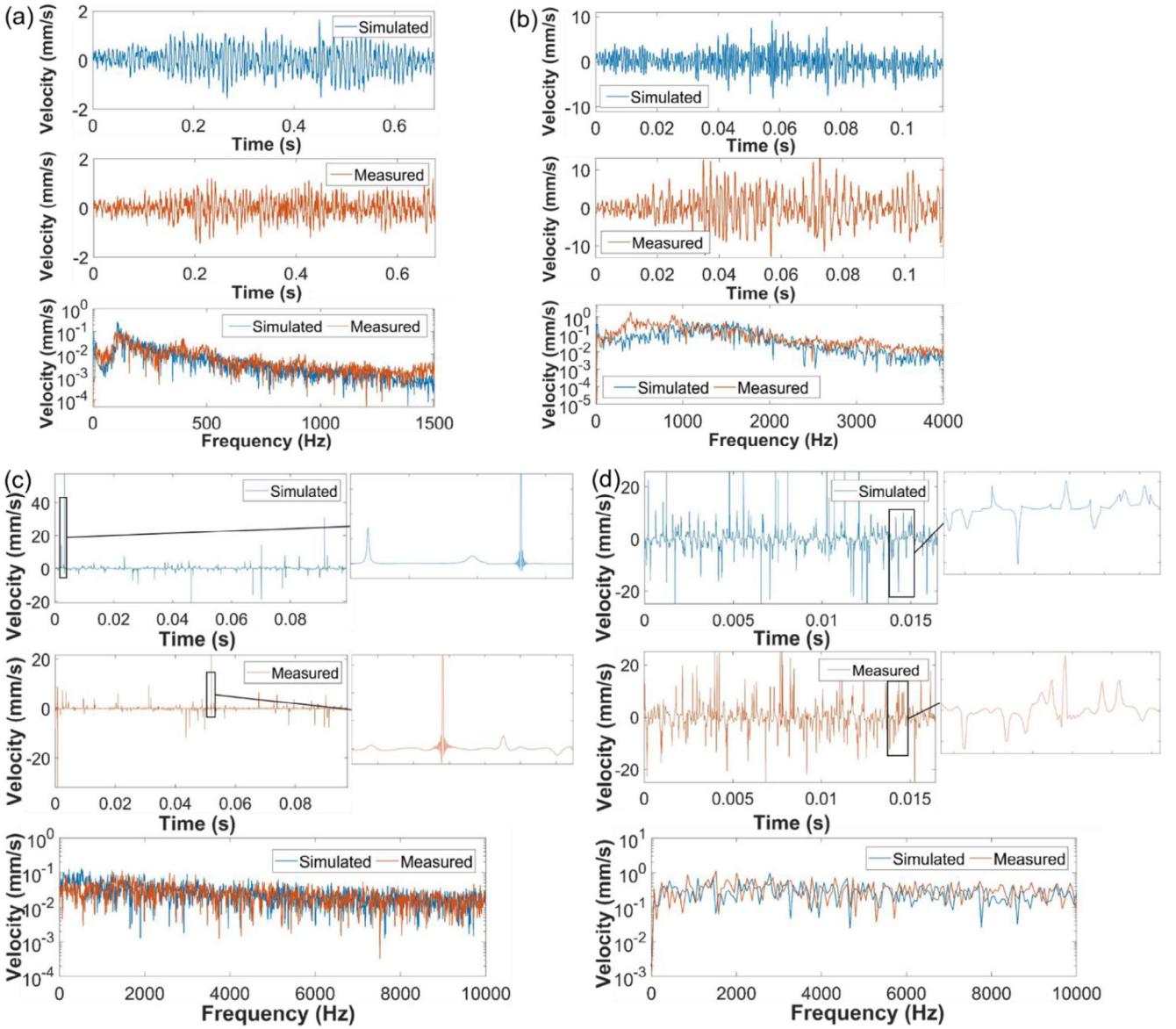

FIGURE 5 Comparisons between simulations and measurements. (a) Sleeper vibrations at 2 km/h; (b) sleeper vibrations at 12 km/h; (c) speckle noise at 2 km/h; (d) speckle noise at 12 km/h.

$cD_1(t)$ is the detail coefficients. Then, find $P\%$ locations in $x_0(t)$ with the largest spike indicators $R_d(t)$ and label them as large spikes.

Step 2. Define an ARIMA model with an autoregressive order p_A, a moving average order q_A, and a differencing order d_A, denoted as ARIMA(p_A, d_A, q_A). Train the ARIMA model with $x_0(t)$ along the forward direction, and replace the labeled points sequentially with predictions from the ARIMA model. Repeat the above training and replacement process along the backward direction. Then, average the forward and backward replacements to obtain the imputed signal $x_1(t)$. The noise component (large spikes) is $\xi_1(t) = x_0(t) - x_1(t)$.

Step 3. Apply a band-pass filter (with the cut-off frequency of f_L and f_H) and a high-pass filter (with the same cut-off frequency f_H) to $x_1(t)$, resulting in the target vibration $x_2(t)$ and the noise component (small spikes) $\xi_2(t)$. Finally, superpose $\xi_1(t)$ with $\xi_2(t)$ as the total noise $\xi(t) = \xi_1(t) + \xi_2(t)$.

The above separation method is illustrated in Figure 6. Steps 1 and 2 aim to extract $P\%$ most influential points (large spikes) from $x_0(t)$ into $\xi_1(t)$, which are usually dominant over a broad frequency range and easier to be separated through time-domain analysis. Specifically, Step 1 calculates spike indicators $R_d(t)$ that represent the noise component in $x_0(t)$ and then labels $P\%$ data points based on their $R_d(t)$. Step 2 then replaces the labeled spikes with

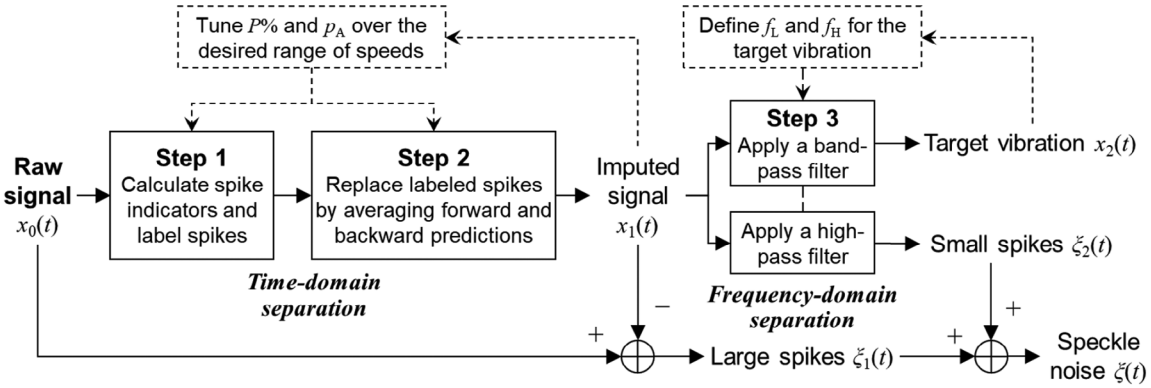

FIGURE 6 Flowchart of the vibration–noise separation method.

predictions from the ARIMA models and takes the difference between the imputed signal $x_1(t)$ and the original signal $x_0(t)$ as the large spikes $\xi_1(t)$. However, changes in train speed lead to changes in spike characteristics. If the actual percentage of large spikes is lower than P%, for example, when the train speed is low, normal data points may be labeled as spikes in Step 1. These points are then replaced in Step 2 by predictions with similar amplitude, thus not affecting $\xi_1(t)$ significantly. If the actual percentage of large spikes is higher than P%, for example, when the train speed is high, some less influential spikes may be retained in $x_1(t)$. Since small spikes are usually at high frequencies, they are filtered out through frequency-domain analysis and then included in $\xi_2(t)$ in Step 3. By combining $\xi_1(t)$ with $\xi_2(t)$, speckle noise is eventually obtained.

The effectiveness of the separation method at various speeds requires a proper selection of its parameters. The most important is the percentage of labeled spikes P% in Step 1, which affects the number of replacements in Step 2. The orders of the ARIMA model (p_A, d_A, q_A) affect the performance of imputation in Step 2. Based on the previous findings (Zeng et al., 2022), it is recommended to set $d_A = 1$ and $q_A = 1$ since they provide good results at different speeds. The parameters P% and p_A should be tuned considering the separation performance and the computational cost over the desired range of speeds. This can be achieved either quantitatively based on simulated signals or qualitatively through trial and observation based on measured signals. Moreover, the cut-off frequencies f_L and f_H in Step 3 are important for separating structural vibrations from residual noise. It is recommended to set them to the lowest and highest frequencies of interest for the target structural vibration, respectively. Procedurally, f_L and f_H can be defined after applying Steps 1 and 2. The above vibration–noise separation method is deeply tied to measurements with LDVs. In this paper, it is used for the vibration measurement of railway sleepers, while it can also be adapted for other applications of structural vibration measurements using LDVs.

3.2 | Parameter tuning with simulations

The simulation models in Section 2 can generate signals of sleeper vibration and speckle noise at different speeds, which makes it possible to quantify the performance of the separation method and tune its parameters. For each sleeper under a certain vehicle speed, the simulated train-borne LDV signal is obtained by superposing the simulated sleeper vibration with the simulated speckle noise. Then, the proposed separation method is applied to the superposed signal, and the separated vibration and noise components are compared with the original vibration and noise signals, respectively. The root-mean-square (RMS) errors and the Pearson correlation coefficient between the separated components and the original signals are calculated to quantify their deviations.

Figure 7a shows the separation performance for a single sleeper using different P% in Step 1. "Raw" represents the result without vibration–noise separation, which yields the largest error and the lowest correlation. "Direct" represents applying solely the filter in Step 3 to the raw signal, which separates some noise in the frequency domain. In cases of $P\% > 0$, the involvement of the time-domain separation in Steps 1 and 2 further improves the performance, and P% in the range of 10%–40% provides low separation errors and high correlation coefficients for both the vibration and the noise at different speeds. When P% is too small, large spikes cannot be effectively extracted in Step 1, so the errors are large. When P% is too large, too many points need to be replaced, resulting in more imputation errors. A similar analysis is performed for the order p_A in Step 2, as shown in Figure 7b. It can be seen that the RMS error and correlation coefficient are not sensitive to p_A as long as $p_A > 5$. However, p_A significantly affects the

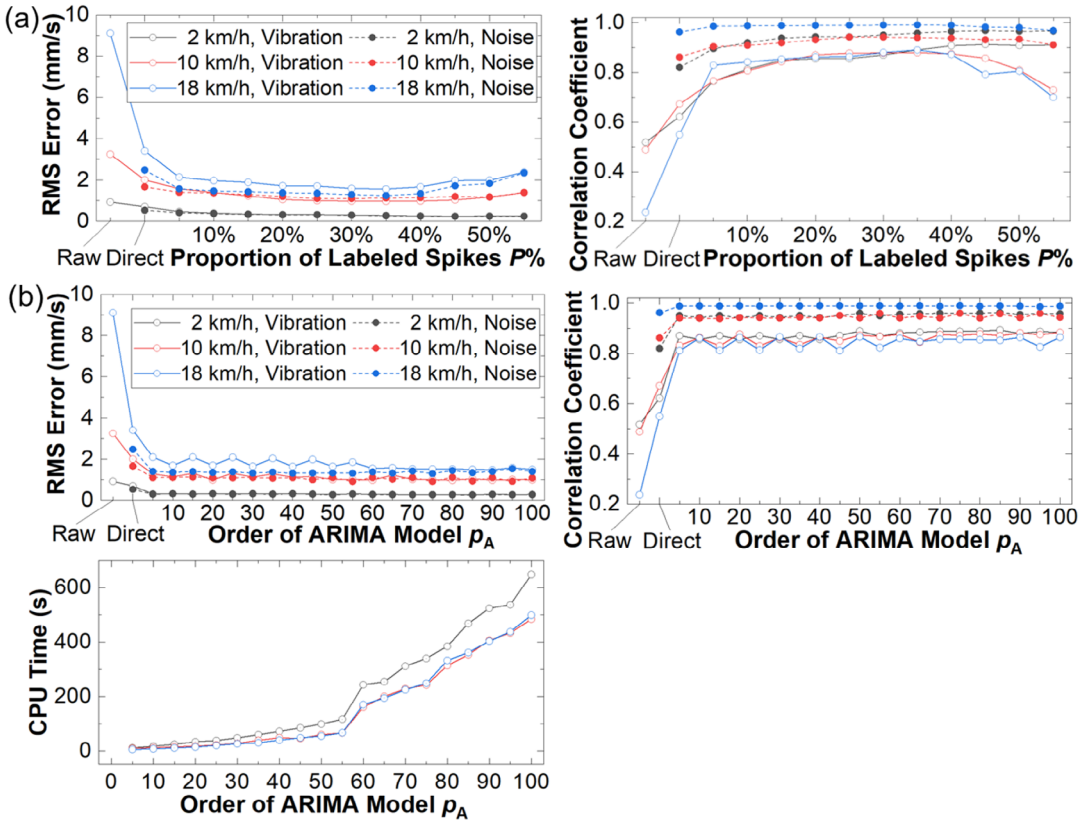

FIGURE 7 Separation performance (when $d_A = 1$, $q_A = 1$, $f_L = 0$ Hz, $f_H = 2000$ Hz). (a) Different $P\%$ (when $p_A = 20$); (b) different p_A (when $P\% = 25\%$).

computational cost, and the higher the p_A, the longer the CPU time (on Intel Xeon E5-2643 with 32 GB RAM).

In this paper, $P\% = 25\%$ and $p_A = 20$ are used as a balance between the separation performance and computational cost. The method is then applied to simulations of the nine sleepers in the middle of the track at different speeds, and the mean and standard deviation of the separation results over the nine sleepers are presented in Table 1. It shows that the separated vibration and noise components are highly correlated with the original signals. Such a high correlation holds at different speeds, and the deviation between the different sleepers is small. This demonstrates the effectiveness of the proposed separation method at different train speeds.

TABLE 1 Separation performance at different speeds.

Speed (km/h)	Correlation coefficient of sleeper vibration		Correlation coefficient of speckle noise	
	Mean	Standard deviation	Mean	Standard deviation
2	.882	.043	.943	.020
4	.782	.075	.949	.024
6	.805	.031	.959	.009
8	.804	.031	.971	.008
10	.849	.027	.974	.013
12	.846	.038	.970	.015
14	.816	.058	.958	.030
16	.828	.061	.962	.015
18	.807	.081	.960	.023
20	.801	.058	.969	.013

3.3 | Validation with laboratory measurements

The separation method is validated with measurements in V-Track. The same parameters in Steps 1 and 2 as Section 3.2 ($P\% = 25\%$, $p_A = 20$, $d_A = 1$, $q_A = 1$) are used. In Step 3, $f_L = 50$ Hz is used to eliminate the effect of the mirror vibration, and $f_H = 1500$ Hz is used to capture the rigid-body motion of the sleepers (Zeng, Shen, et al., 2023). The separation results for a typical sleeper at different speeds are shown in Figure 8. As the speed increases, the signal length becomes shorter, and the frequency resolution becomes lower. By comparing the raw and imputed signals, it can be seen that large spikes are separated after Steps 1 and 2, while small spikes remain to be separated

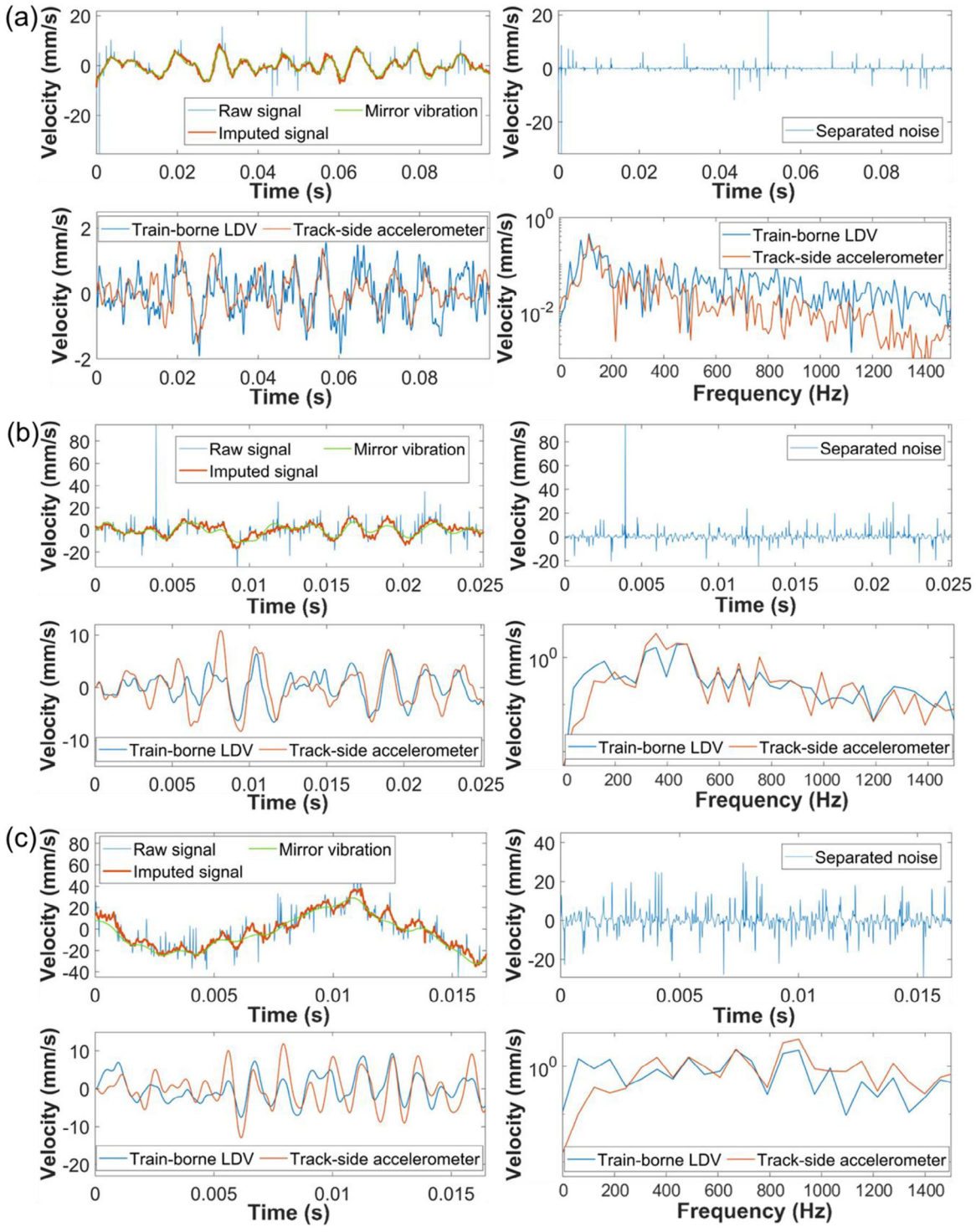

FIGURE 8 Separation results and comparisons with trackside measurements at different speeds. (a) 2 km/h, (b) 8 km/h, (c) 12 km/h.

in Step 3. Additionally, the mirror vibration dominates the low frequencies and is filtered out in Step 3.

Generally, the separated noise is very close to that in the raw signals. Meanwhile, the sleeper vibrations separated from the train-borne LDV signals are consistent with those measured by the trackside accelerometer in both time and frequency domains. These results demonstrate the measuring capability of the train-borne LDV and the effectiveness of the proposed method at different speeds. Some residual noise can be noticed in the separated sleeper vibration, which is less pronounced at higher speeds due to increased vibration amplitude and frequency. The deviations between the train-borne LDV signals and the trackside accelerometer signals are caused

by imperfect separation and the spatial deviations between the laser spot and the accelerometers.

It should be noted that the train-borne LDV and the trackside accelerometers measure both pass-by vibrations (caused by the moving vehicle) and ambient vibrations in the laboratory. The influence of ambient vibrations on the fidelity of the pass-by vibration measurement is considered negligible in our case study since there are no major vibration sources in the vicinity during the measurement.

4 | APPLICATION TO FIELD MEASUREMENTS

Since the above simulations and laboratory measurements represent scaled and simplified vehicle-track systems, field measurements are necessary to further test the train-borne LDV technology and the vibration–noise separation method in the real world. It is implemented on the CTO measurement train of TU Delft, as shown in Figure 9a. The same LDV used in the laboratory is installed in the cabin, and its laser beam is targeted at sleepers (and ballast) through a hole in the cabin floor. Two accelerometers (PCB 356B21) are installed on the LDV to measure its vibration, and a camera is used to record the trajectory of the laser spot on track structures.

Since the vibration signals and the video frames are stored separately at different sampling rates, they need to be synchronized. We align them by using some unique objects in the track (e.g., joints and crossings) as references. These objects are identifiable in both signals, and the alignments at different reference locations are further averaged. The synchronization accuracy is sufficient in our case study considering the short length of the signals (less than 60 s per track section). If a long measurement (e.g., several hours) is considered, the synchronization becomes more challenging since timing errors between different systems accumulate and simply aligning signals is not sufficient. In this case, more advanced strategies are needed to tackle the challenges.

The measurements are conducted on an operational railway track in Rotterdam, the Netherlands, as shown in Figure 9b. It is a typical ballasted track with concrete sleepers. The CTO train is pulled by a locomotive connected to the LDV side. The measurements at speeds below 30 km/h are focused on since higher speeds cause more significant motion blur, which induces more challenges in accurately positioning the laser spot on each individual sleeper.

Figure 9c and d show the results measured in two typical sections. The upper plots show the change in train speeds with respect to sleeper numbers, in which the speed is estimated by assuming a uniform sleeper spacing. The LDV signal is cut into segments for each sleeper, and the

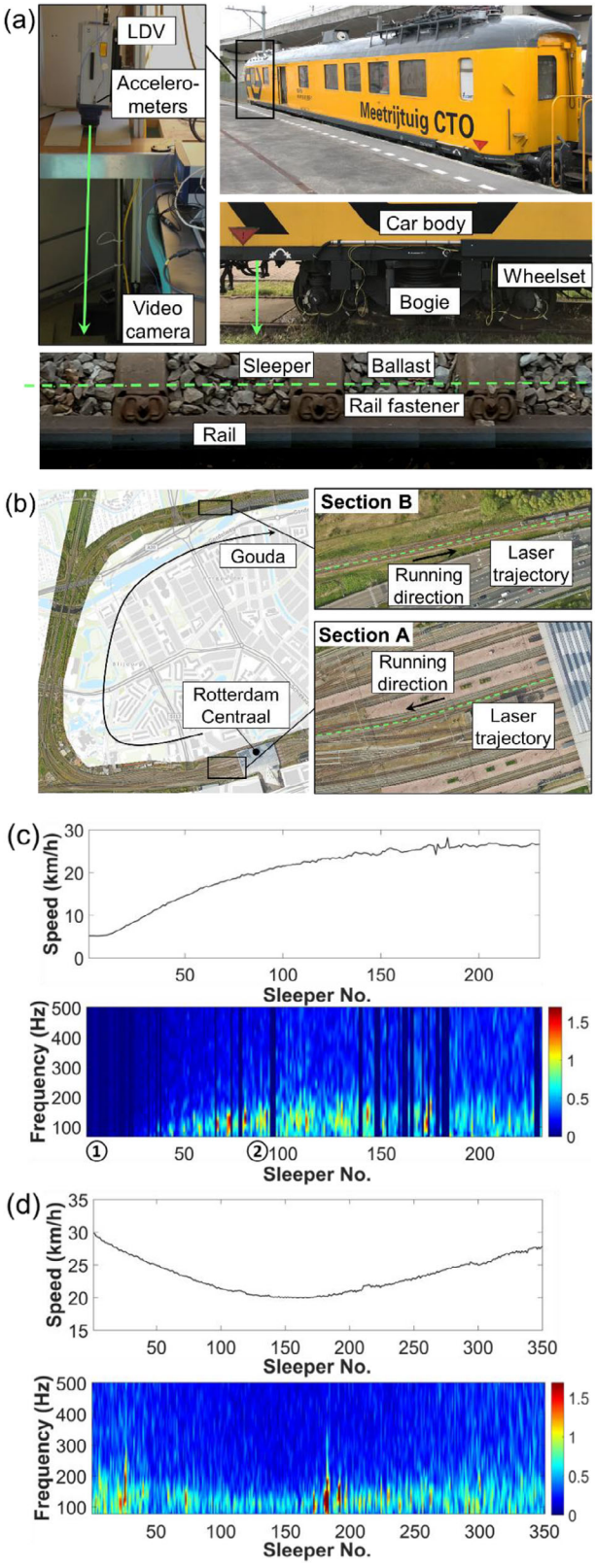

FIGURE 9 Field measurements. (a) CTO train instrumented with a laser Doppler vibrometer (LDV); (b) train route and two selected sections (aerial photographs used from GeoInformatie Portaal of ProRail https://maps.prorail.nl/); (c) train speed and spectrum of imputed signal for each sleeper in Section A; (d) train speed and spectrum of imputed signal for each sleeper in Section B.

vibration–noise separation method (with the same parameters in Steps 1 and 2 as in Sections 3.2 and 3.3) is applied to each segment. The lower plots show by a colored strip the Fourier spectrum of the imputed signal (after Steps 1 and 2) for each sleeper. It can be seen that the amplitude of the sleeper vibration increases with the increase in speed. A higher speed generates more excitations at higher frequencies, thus leading to larger vibration responses at higher frequencies. The dominant frequency of the sleeper vibration is generally below 300 Hz, which is consistent with the frequency range of rigid-body motions and first-order bending of in situ sleepers (Shen et al., 2021; Zeng, Shen, et al., 2023). Therefore, $f_{\mathrm{H}} = 300$ Hz is used in Step 3. It is noteworthy that f_{H} differs significantly between the field and laboratory measurements due to the different natural frequencies of the sleepers. Additionally, $f_{\mathrm{L}} = 80$ Hz is used to eliminate the influence of the LDV vibration.

Two sleepers are further selected to showcase the vibration–noise separation performance, as plotted in Figure 10. Sleeper ① is measured at 6 km/h, where the LDV vibration dominates the raw signal and the amplitude of the extracted sleeper vibration is small. Sleeper ② is measured at 21 km/h, and the amplitude and dominant frequency of the sleeper vibration are significantly higher than those of the LDV vibration. Meanwhile, the amplitudes of the extracted sleeper vibration and speckle noise are both larger than those of Sleeper ①. In general, the proposed separation method effectively reduces the speckle noise in the raw signals and captures the dominant sleeper vibrations at different speeds. Unfortunately, we were not able to access the track to conduct trackside measurements to further verify the results.

It is worth noting that the same parameters for vibration–noise separation in Steps 1 and 2 work effectively under different scenarios, including simulations (up to 20 km/h), laboratory measurements (up to 12 km/h), and field measurements (up to 30 km/h). In addition, the performance is not sensitive to the variation in signal length due to the variation in speed. This reflects the generalization capability of the proposed method, at least under the tested scenarios and speeds.

5 | SPEED-DEPENDENT CHARACTERISTICS

SNR is a key indicator representing the quality and usability of a measured signal. It quantifies how pronounced the real vibration is with respect to the noise, calculated based on their RMS values as follows:

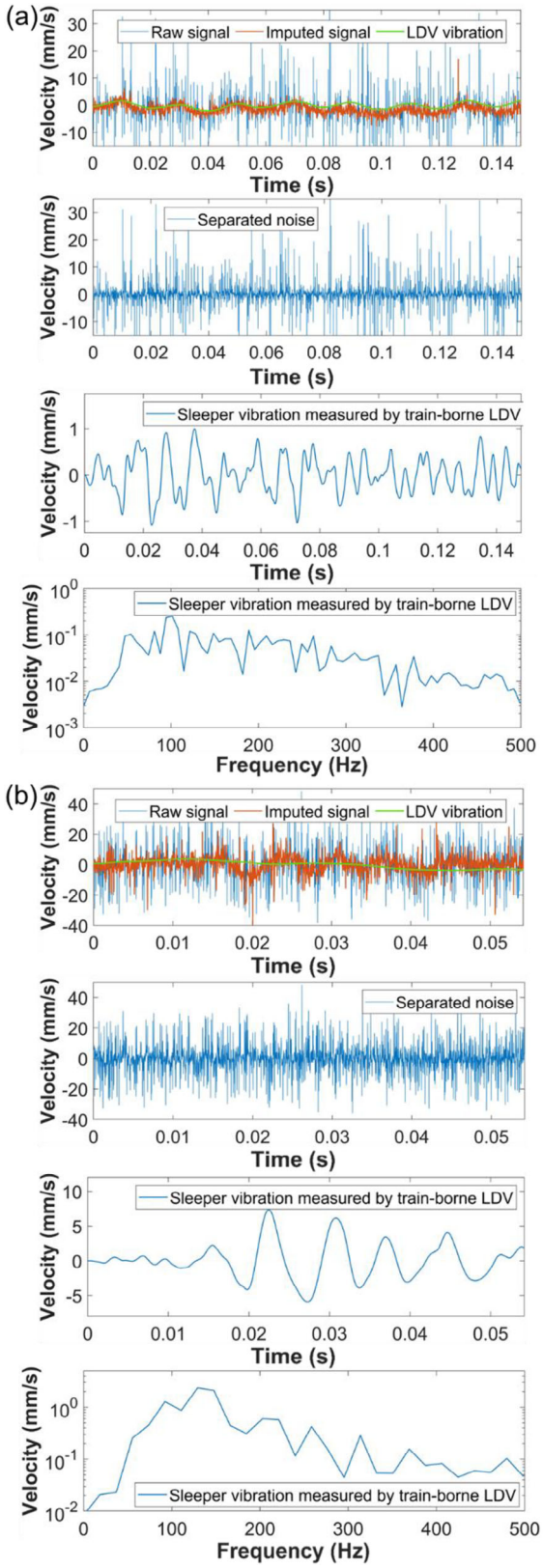

FIGURE 10 Separation results of two sleepers. (a) Sample ①, (b) Sample ②.

$$SNR = 20 \log_{10} \left(\frac{\mathrm{RMS}\left(\dot{z}(t)\right)}{\mathrm{RMS}\left(\xi(t)\right)} \right) \tag{13}$$

To investigate the influence of train speed on sleeper vibrations and speckle noise and further on the SNR of train-borne LDV measurements, the SNRs at different speeds are calculated based on the simulations, laboratory measurements, and field measurements. In the simulation scenario, sleeper vibrations and speckle noise are simulated separately so the SNRs can be accurately obtained. For the laboratory and field measurements, sleeper vibrations and speckle noise are separated from the LDV signals using the method in Section 3, and the SNR can only be an estimation.

5.1 | Simulations

In the simulation study, the stiffness and damping of rail pads and ballast are assumed to follow Gaussian distributions as a consideration of uncertainties in the track properties. For each parameter, the mean is its nominal value in Table A1, and the standard deviation is 5% of the nominal value. Random numbers following these distributions are generated for each sleeper. Figure 11a first shows the simulation results for the nine sleepers in the middle of the track, in which the RMS value is calculated based on the response of each sleeper when the wheel is within ±1.5 sleeper spacing from it. As the speed increases, the sleeper vibration becomes larger, with the slope first increasing and then decreasing, and the standard deviation over the nine sleepers also increases. According to Equation (6), the train-borne LDV captures only a fragment of the sleeper vibration response under the wheel passage, and the higher the speed, the shorter the fragment. Figure 11a then shows the RMS values of the fragments measured on the nine sleepers. The measured sleeper vibrations increase with speed, following the same trend as in the first plot. The standard deviation also increases with increasing speed. The deviation between the sleepers is more pronounced when measuring with the train-borne LDV, which reflects larger uncertainties due to the shorter length of the measured sleeper response.

Then, nine simulations of speckle translation are performed at each speed, corresponding to the measurements on the nine sleepers. The results in Figure 11a show that the RMS value of the speckle noise increases almost linearly with the increasing speed while its standard deviation becomes larger. Further, the SNR is calculated for each sleeper, as shown in the last plot of Figure 11a. A significant nonlinear behavior can be observed as a result of the competition between the linear increase of the speckle noise and the nonlinear increase of the sleeper vibration with respect to the increasing speed. At low speeds, the sleeper vibration is too small while the speckle noise increases faster, so the SNR first decreases and reaches a local minimum at around 4 km/h. Then, as the sleeper vibration increases more steeply than the speckle noise, the SNR starts to increase and reaches a local maximum at 10–15 km/h. Further, as the sleeper vibration increases more slowly, the SNR drops gradually as the speed increases.

5.2 | Laboratory measurements

The vibration–noise separation method is applied to measurements in V-Track at different running laps (rotations of the beam). The RMS values of the separated vibration and speckle noise as well as the SNR are calculated for each sleeper (excluding those near the joints). Figure 11b shows their box plot distributions at different speeds. It can be seen from the data points and their percentiles that the sleeper vibration and speckle noise exhibit more significant deviations between sleepers than the simulation results in Figure 11a. Such a deviation is caused by uncertainties in the sleeper dynamics, the track geometry, and the laser speckle and becomes more pronounced as the speed increases.

Despite the uncertainties, the mean and median in the first plot of Figure 11b show that as the speed increases, the sleeper vibration increases with larger slopes between 4 and 10 km/h. The measured RMS values are close to the simulation result in Figure 11a. Meanwhile, Figure 11b shows that the speckle noise increases almost linearly with speed, which is consistent with the simulation result. These agreements reflect that the established models effectively characterize the track dynamics and the speckle noise in V-Track. Further, the last plot of Figure 11b shows that, as the speed increases, the SNR first increases (2–6 km/h), becomes flat (6–10 km/h), and then decreases slightly (10–12 km/h). This result is similar to the simulated trend above 4 km/h in Figure 11a, while deviation occurs at 2 km/h because the RMS values are relatively small and the SNR is sensitive to slight deviations between simulations and measurements.

5.3 | Field measurements

In the field measurements, considering the potential error in synchronizing the LDV signal with the laser spot position, the measured signal is cut into overlapped segments with different offsets from the estimated center of each sleeper, as shown in Figure 12. Then, for each segment, the vibration–noise separation method is applied, and the RMS values of the sleeper vibration and speckle noise and the corresponding SNR are calculated. Finally, the

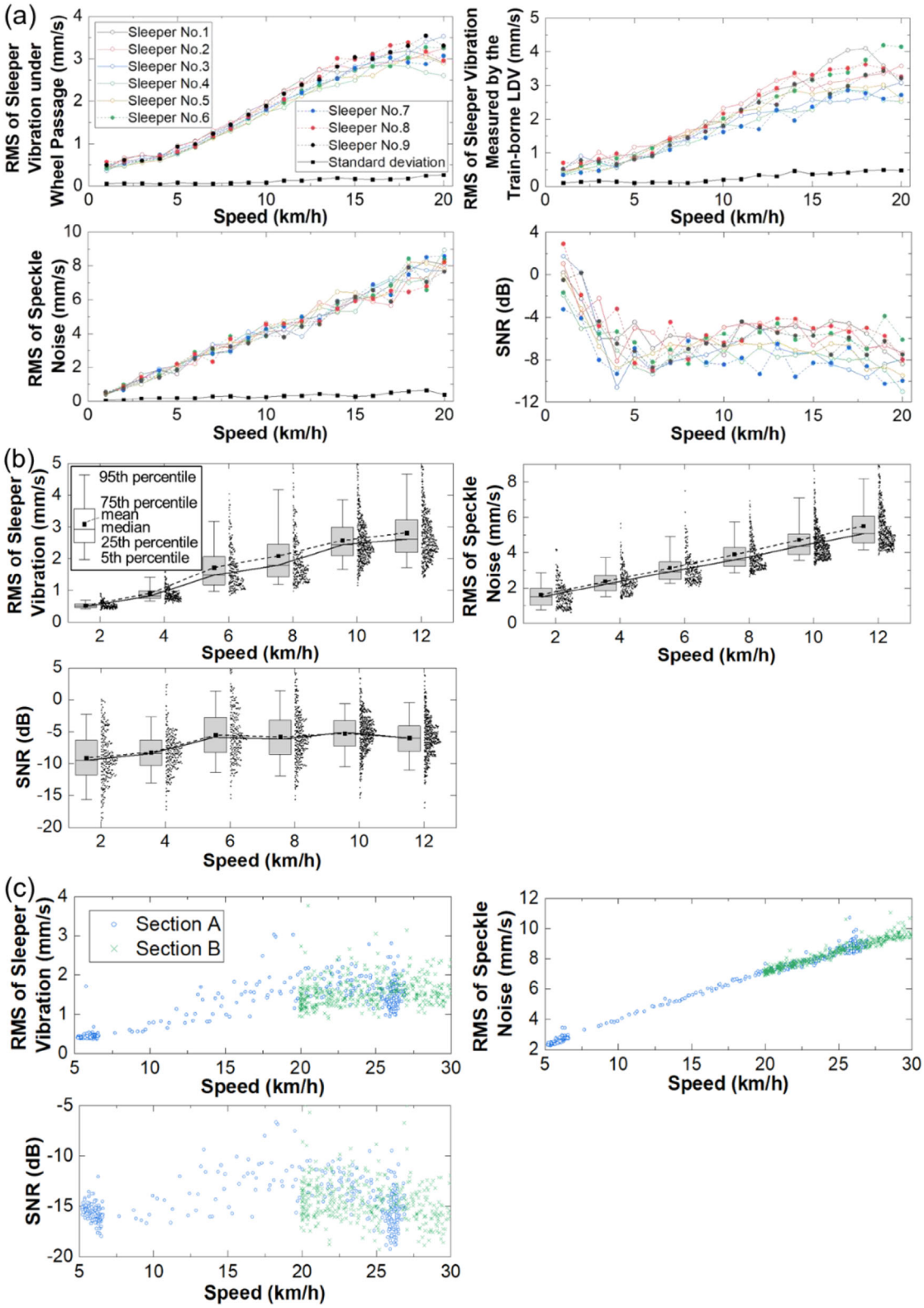

FIGURE 11 Speed-dependent characteristics. (a) Simulations, (b) laboratory measurements, (c) field measurements.

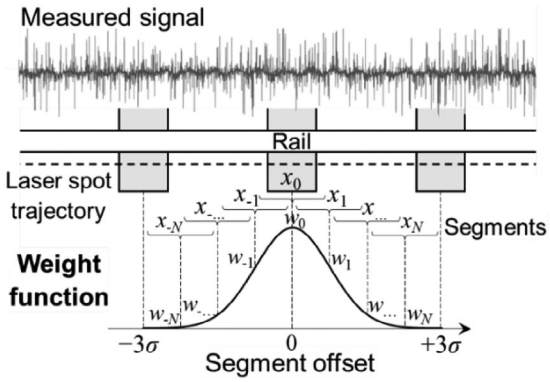

FIGURE 12 Weight assignment for segments with different offsets.

weighted average of the results from different segments for each sleeper is calculated as the final result. The weights follow the shape of a Gaussian distribution and decrease toward zero as the segment offsets from the estimated center to the adjacent sleepers.

The results for all the 580 sleepers in Figure 9c and d are plotted in Figure 11c. It shows trends similar to the simulation and laboratory measurement results in Figure 11a and b. As the speed increases, the sleeper vibration increases first slowly (5–10 km/h), then rapidly (10–20 km/h), then slowly again and even drops slightly (20–30 km/h). Meanwhile, the speckle noise amplitude increases almost linearly with respect to the speed. As a consequence of the competition between the sleeper vibration and the speckle noise, the SNR first drops slightly to reach a local minimum at 7 km/h, then increases to reach a local maximum at 20 km/h, and then drops gradually. Within the speed range investigated, the speed of 15–25 km/h provides a higher SNR than others.

The similarity between the above simulation, laboratory measurement, and field measurement results demonstrates that the proposed methodology effectively characterizes the speed-dependent characteristics of train-borne LDV measurements. Nevertheless, it should be noted that the change of SNR with respect to speed depends on the characteristics of sleeper dynamics and speckle noise. Therefore, the optimal speed with the highest SNR varies for different tack structures, measurement configurations, and operational conditions.

6 | CONCLUSION

This paper proposes and applies a holistic methodology to characterize train-borne LDV measurements for sleeper vibrations and investigates their speed-dependent characteristics. Validated numerical models are used to separately simulate sleeper vibrations and speckle noise at different speeds and support the parameter tuning of the developed vibration–noise separation method. The method is then validated with laboratory measurements and applied to field measurements. The dependence of sleeper vibration, speckle noise, and SNR on train speed is determined using simulations and measurements. The main conclusions are summarized below.

(1) The established train-track-LDV model and speckle translation model reproduce the sleeper vibrations and speckle noise in V-Track at the vehicle speed of 2–12 km/h.
(2) The vibration–noise separation method works effectively in the simulations at the speed of 1–20 km/h, the laboratory measurements at the speed of 2–12 km/h, and the field measurements at the speed of 5–30 km/h.
(3) The RMS value of speckle noise increases almost linearly with speed, whereas the RMS value of sleeper vibration increases nonlinearly with speed. Their competition leads to the nonlinear behavior of SNR with respect to train speed. The optimal speed range yielding the highest SNR varies for different tack structures and measurement configurations, for example, 6–10 km/h in the laboratory measurements and 15–25 km/h in the field measurements.

This paper demonstrates the potential of train-borne LDV to be applied to large-scale rail infrastructure monitoring. Analyzing its speed-dependent characteristics provides deeper insights into the quality and usability of signals measured at different speeds. With the simulations serving as the foundation and assurance for this research, future research will focus more on real-life measurements. The vibration–noise separation method will be improved by incorporating signal processing methods that are potentially more effective for strongly nonstationary signals, such as synchrosqueezed wavelet transform (Amezquita-Sanchez & Adeli, 2015a; Li et al., 2017; Perez-Ramirez et al., 2016), Bayesian wavelet transform (Jiang et al., 2007; Yue et al., 2019), and empirical wavelet transform (Amezquita-Sanchez & Adeli, 2015b; Hu et al., 2017). Field measurements, including both train-borne and track-side measurements, will be performed to further verify the technology. The performance of train-borne LDV measurements at higher speeds will also be investigated, where higher frequency bands, more uncertainties, and lower frequency resolution can be expected.

Furthermore, it can be noticed from the real-life measurements that different sleepers vibrate differently, which is related to the properties of the sleepers and other track components, such as rail pads and ballast. Therefore, the measured sleeper vibrations can be used to monitor the dynamic properties of track structures. To tackle the challenge induced by the amplitude and frequency variation of the excitation from the vehicle to the track,

wheel-rail force or vehicle vibration signals can be incorporated to normalize the train-borne LDV signals and estimate the transfer functions of track structures (Zeng, Núñez, et al., 2023). The deviation in the estimated transfer functions can reflect the difference in track stiffness and damping, which can be further used for anomaly detection in railway tracks.

ACKNOWLEDGMENTS

This research was partly supported by ProRail and the Project Reliable Embankments for Safe Expansion in Rail Traffic (RESET). The authors thank Jan Moraal, Jurjen Hendriks, Li Wang, and Fang Ren for their help in the laboratory and field measurements. Special thanks go to the reviewers for their detailed and valuable comments.

REFERENCES

Allen, M. S., & Sracic, M. W. (2010). A new method for processing impact excited continuous-scan laser Doppler vibrometer measurements. *Mechanical Systems and Signal Processing*, *24*(3), 721–735.

Amezquita-Sanchez, J. P., & Adeli, H. (2015). Synchrosqueezed wavelet transform-fractality model for locating, detecting, and quantifying damage in smart highrise building structures. *Smart Materials and Structures*, *24*(6), 065034.

Amezquita-Sanchez, J. P., & Adeli, H. (2015). A new music-empirical wavelet transform methodology for time–frequency analysis of noisy nonlinear and non-stationary signals. *Digital Signal Processing*, *45*, 55–68.

Amezquita-Sanchez, J. P., & Adeli, H. (2016). Signal processing techniques for vibration-based health monitoring of smart structures. *Archives of Computational Methods in Engineering*, *23*, 1–15.

Amezquita-Sanchez, J. P., & Adeli, H. (2019). Nonlinear measurements for feature extraction in structural health monitoring. *Scientia Iranica*, *26*(6), 3051–3059.

Aranchuk, V., Lal, A. K., Hess, C. F., Sabatier, J. M., Burgett, R. D., Aranchuk, I., & Mayo Jr, W. T. (2006). Speckle noise in a continuously scanning multibeam laser Doppler vibrometer for acoustic landmine detection. *Detection and Remediation Technologies for Mines and Minelike Targets XI*, *6217*, 366–375.

Arruda, J., Vianna do Rio, S. A., & Bernardes Santos, L. A. S. (1996). A space-frequency data compression method for spatially dense laser Doppler vibrometer measurements. *Shock and Vibration*, *3*(2), 127–133.

Asakura, T., & Takai, N. (1981). Dynamic laser speckles and their application to velocity measurements of the diffuse object. *Applied Physics*, *25*(3), 179–194.

Auersch, L. (2006). Ground vibration due to railway traffic—The calculation of the effects of moving static loads and their experimental verification. *Journal of Sound and Vibration*, *293*(3-5), 599–610.

Berggren, E. G., Nissen, A., & Paulsson, B. S. (2014). Track deflection and stiffness measurements from a track recording car. *Proceedings of the Institution of Mechanical Engineers, Part F: Journal of Rail and Rapid Transit*, *228*(6), 570–580.

Bian, X., Jiang, H., Chang, C., Hu, J., & Chen, Y. (2015). Track and ground vibrations generated by high-speed train running on ballastless railway with excitation of vertical track irregularities. *Soil Dynamics and Earthquake Engineering*, *76*, 29–43.

Bocciolone, M., Caprioli, A., Cigada, A., & Collina, A. (2007). A measurement system for quick rail inspection and effective track maintenance strategy. *Mechanical Systems and Signal Processing*, *21*(3), 1242–1254.

Boogaard, M. A., Li, Z., & Dollevoet, R. (2018). In situ measurements of the crossing vibrations of a railway turnout. *Measurement*, *125*, 313–324.

Brandt, A., & Brincker, R. (2014). Integrating time signals in frequency domain—Comparison with time domain integration. *Measurement*, *58*, 511–519.

Chen, D. M., Xu, Y. F., & Zhu, W. D. (2018). Identification of damage in plates using full-field measurement with a continuously scanning laser Doppler vibrometer system. *Journal of Sound and Vibration*, *422*, 542–567.

Denman, M., Halliwell, N. A., & Rothberg, S. J. (1996). Speckle noise reduction in laser vibrometry: Experimental and numerical optimisation. In Enrico Primo Tomasini (ed.), *Second international conference on vibration measurements by laser techniques: Advances and applications* (pp. 280–291), SPIE Digital Library, Bellingham, USA.

Di Maio, D., Castellini, P., Martarelli, M., Rothberg, S., Allen, M. S., Zhu, W. D., & Ewins, D. J. (2021). Continuous scanning laser vibrometry: A raison d'être and applications to vibration measurements. *Mechanical Systems and Signal Processing*, *156*, 107573.

Hu, Y., Li, F., Li, H., & Liu, C. (2017). An enhanced empirical wavelet transform for noisy and non-stationary signal processing. *Digital Signal Processing*, *60*, 220–229.

Jiang, X., Mahadevan, S., & Adeli, H. (2007). Bayesian wavelet packet denoising for structural system identification. *Structural Control and Health Monitoring*, *14*(2), 333–356.

Jin, Y., Dollevoet, R., & Li, Z. (2022). Numerical simulation and characterization of speckle noise for laser Doppler vibrometer on moving platforms (LDVom). *Optics and Lasers in Engineering*, *158*, 107135.

Jin, Y., Dollevoet, R., & Li, Z. (2022). Removing speckle noise from the signals of a laser Doppler vibrometer on moving platforms (LDVom) by ensemble empirical mode decomposition. *Measurement Science and Technology*, *33*(12), 125205.

Jin, Y., & Li, Z. (2022). Mitigating speckle noise in a laser Doppler vibrometer using Fourier analysis. *Optics Letters*, *47*(18), 4742–4745.

Karim, A., & Adeli, H. (2002). Incident detection algorithm using wavelet energy representation of traffic patterns. *Journal of Transportation Engineering*, *128*(3), 232–242.

Katicha, S. W., Flintsch, G., Bryce, J., & Ferne, B. (2014). Wavelet denoising of TSD deflection slope measurements for improved pavement structural evaluation. *Computer-Aided Civil and Infrastructure Engineering*, *29*(6), 399–415.

Kaynardag, K., Battaglia, G., Ebrahimkhanlou, A., Pirrotta, A., & Salamone, S. (2021). Identification of bending modes of vibration in rails by a laser Doppler vibrometer on a moving platform. *Experimental Techniques*, *45*(1), 13–24.

Kaynardag, K., Yang, C., & Salamone, S. (2023). A rail defect detection system based on laser Doppler vibrometer measurements. *NDT & E International*, *137*, 102858.

Le Pen, L., Milne, D., Thompson, D., & Powrie, W. (2016). Evaluating railway track support stiffness from trackside measurements in the absence of wheel load data. *Canadian Geotechnical Journal*, *53*(7), 1156–1166.

Li, C., He, Q., & Wang, P. (2022). Estimation of railway track longitudinal irregularity using vehicle response with information compression and Bayesian deep learning. *Computer-Aided Civil and Infrastructure Engineering*, *37*(10), 1260–1276.

Li, J., & Shi, H. (2019). Rail corrugation detection of high-speed railway using wheel dynamic responses. *Shock and Vibration*, *2019*, Article ID 2695647.

Li, Z., Molodova, M., Núñez, A., & Dollevoet, R. (2015). Improvements in axle box acceleration measurements for the detection of light squats in railway infrastructure. *IEEE Transactions on Industrial Electronics*, *62*(7), 4385–4397.

Li, Z., Park, H. S., & Adeli, H. (2017). New method for modal identification of super high-rise building structures using discretized synchrosqueezed wavelet and Hilbert transforms. *The Structural Design of Tall and Special Buildings*, *26*(3), e1312.

Liu, G., Li, P., Wang, P., Liu, J., Xiao, J., Chen, R., & Wei, X. (2021). Study on structural health monitoring of vertical vibration of ballasted track in high-speed railway. *Journal of Civil Structural Health Monitoring*, *11*(2), 451–463.

Lutzmann, P., Göhler, B., Van Putten, F., & Hill, C. A. (2011). Laser vibration sensing: overview and applications. *Electro-Optical Remote Sensing, Photonic Technologies, and Applications V*, *8186*, 11–26.

Lv, T., Han, X., Wu, S., & Li, Y. (2019). The effect of speckles noise on the laser Doppler vibrometry for remote speech detection. *Optics Communications*, *440*, 117–125.

Martarelli, M. (2001). *Exploiting the laser scanning facility for vibration measurements*. University of London.

Martarelli, M., & Ewins, D. J. (2006). Continuous scanning laser Doppler vibrometry and speckle noise occurrence. *Mechanical Systems and Signal Processing*, *20*(8), 2277–2289.

Martin, P., & Rothberg, S. (2009). Introducing speckle noise maps for laser vibrometry. *Optics and Lasers in Engineering*, *47*(3-4), 431–442.

Milne, D. R. M., Le Pen, L. M., Thompson, D. J., & Powrie, W. (2017). Properties of train load frequencies and their applications. *Journal of Sound and Vibration*, *397*, 123–140.

Molodova, M., Li, Z., & Dollevoet, R. (2008). An investigation of the possibility to use axle box acceleration for condition monitoring of welds. *ISMA*, *2008*, 2879–2886.

Molodova, M., Oregui, M., Núñez, A., Li, Z., & Dollevoet, R. (2016). Health condition monitoring of insulated joints based on axle box acceleration measurements. *Engineering Structures*, *123*, 225–235.

Muramatsu, M., Uchida, S., & Takahashi, Y. (2020). Non-contact detection of concrete flaws by neural network classification of laser Doppler vibrometer signals. *Engineering Research Express*, *2*(2), 025017.

Naeimi, M., Li, Z., Petrov, R. H., Sietsma, J., & Dollevoet, R. (2018). Development of a new downscale setup for wheel-rail contact experiments under impact loading conditions. *Experimental Techniques*, *42*(1), 1–17.

Newmark, N. M. (1959). A method of computation for structural dynamics. *Journal of the Engineering Mechanics Division*, *85*(3), 67–94.

OBrien, E. J., & Malekjafarian, A. (2016). A mode shape-based damage detection approach using laser measurement from a vehicle crossing a simply supported bridge. *Structural Control and Health Monitoring*, *23*(10), 1273–1286.

Park, S. W., Park, H. S., Kim, J. H., & Adeli, H. (2015). 3D displacement measurement model for health monitoring of structures using a motion capture system. *Measurement*, *59*, 352–362.

Perez-Ramirez, C. A., Amezquita-Sanchez, J. P., Adeli, H., Valtierra-Rodriguez, M., Camarena-Martinez, D., & Romero-Troncoso, R. J. (2016). New methodology for modal parameters identification of smart civil structures using ambient vibrations and synchrosqueezed wavelet transform. *Engineering Applications of Artificial Intelligence*, *48*, 1–12.

Rahimi, S., Li, Z., & Dollevoet, R. (2014). Measuring with laser Doppler vibrometer on moving frame (LDVMF). *AIVELA 2014*, *1600*, 274–286.

Revel, G. M., Castellini, P., Chiariotti, P., Tomasini, E. P., Cenedese, F., & Perazzolo, A. (2011). Laser vibrometry vibration measurements on vehicle cabins in running conditions: Helicopter mock-up application. *Optical Engineering*, *50*(10), 101502.

Rothberg, S. (2006). Numerical simulation of speckle noise in laser vibrometry. *Applied Optics*, *45*(19), 4523–4533.

Rothberg, S. J., Allen, M. S., Castellini, P., Di Maio, D., Dirckx, J. J. J., Ewins, D. J., Halkon, B. J., Muyshondt, P., Paone, N., Ryan, T., Steger, H., Tomasini, E. P., Vanlanduit, S., & Vignola, J. F. (2017). An international review of laser Doppler vibrometry: Making light work of vibration measurement. *Optics and Lasers in Engineering*, *99*, 11–22.

Rothberg, S. J., & Halkon, B. J. (2004). Laser vibrometry meets laser speckle. *Sixth International Conference on Vibration Measurements by Laser Techniques: Advances and Applications*, *5503*, 280–291.

Rothberg, S. J., & Tirabassi, M. (2012). A universal framework for modelling measured velocity in laser vibrometry with applications. *Mechanical Systems and Signal Processing*, *26*, 141–166.

Salvador, P., Naranjo, V., Insa, R., & Teixeira, P. (2016). Axlebox accelerations: Their acquisition and time–frequency characterisation for railway track monitoring purposes. *Measurement*, *82*, 301–312.

Sels, S., Vanlanduit, S., Bogaerts, B., & Penne, R. (2019). Three-dimensional full-field vibration measurements using a handheld single-point laser Doppler vibrometer. *Mechanical Systems and Signal Processing*, *126*, 427–438.

Shen, C., Dollevoet, R., & Li, Z. (2021). Fast and robust identification of railway track stiffness from simple field measurement. *Mechanical Systems and Signal Processing*, *152*, 107431.

Shen, C., Li, Z., & Dollovoet, R. (2019). A novel method for railway crossing monitoring based on ambient vibration caused by train-track interaction. *IAVSD*, *2019*, 133–141.

Siringoringo, D. M., & Fujino, Y. (2009). Non-contact operational modal analysis of structural members by laser Doppler vibrometer. *Computer-Aided Civil and Infrastructure Engineering*, *24*(4), 249–265.

Sracic, M. W., & Allen, M. S. (2009). Experimental investigation of the effect of speckle noise on continuous scan laser Doppler vibrometer measurements. In *In 27th International Modal Analysis Conference (IMAC XXVII)*, Florida, USA, February 2009.

Sresakoolchai, J., & Kaewunruen, S. (2022). Prognostics of unsupported railway sleepers and their severity diagnostics using machine learning. *Scientific Reports*, *12*(1), 1–10.

Stanbridge, A. B., Martarelli, M., & Ewins, D. J. (2004). Measuring area vibration mode shapes with a continuous-scan LDV. *Measurement*, *35*(2), 181–189.

Wang, P., Wang, L., Chen, R., Xu, J., Xu, J., & Gao, M. (2016). Overview and outlook on railway track stiffness measurement. *Journal of Modern Transportation*, *24*(2), 89–102.

Wang, Y., Zhang, W., Wu, Z., Kong, X., & Zhang, H. (2021). Speckle noise detection and removal for laser speech measurement systems. *Applied Sciences*, *11*(21), 9870.

Wei, Z., Núñez, A., Li, Z., & Dollevoet, R. (2017). Evaluating degradation at railway crossings using axle box acceleration measurements. *Sensors*, *17*(10), 2236.

Xu, Y. F., Chen, D. M., & Zhu, W. D. (2017). Damage identification of beam structures using free response shapes obtained by use of a continuously scanning laser Doppler vibrometer system. *Mechanical Systems and Signal Processing*, *92*, 226–247.

Yang, Z., Boogaard, A., Chen, R., Dollevoet, R., & Li, Z. (2018). Numerical and experimental study of wheel-rail impact vibration and noise generated at an insulated rail joint. *International Journal of Impact Engineering*, *113*, 29–39.

Yue, G. D., Xu, Z., Wang, L., Liu, C., & Ren, T. (2016). WSN-based vibration characteristic research for various railway track structures for pattern classification. *International Journal of Pattern Recognition and Artificial Intelligence*, *30*(10), 1650020.

Yue, G. D., Xu, Z., Wang, L. D., Liu, C., & Zhou, W. J. (2017). Vibration analysis for slab track at different train speeds using Bayes wavelet denoising. *Proceedings of the Institution of Mechanical Engineers, Part F: Journal of Rail and Rapid Transit*, *231*(8), 892–901.

Yue, G. D., Cui, X. S., Zou, Y. Y., Bai, X. T., Wu, Y. H., & Shi, H. T. (2019). A Bayesian wavelet packet denoising criterion for mechanical signal with non-Gaussian characteristic. *Measurement*, *138*, 702–712.

Zeng, Y., Núñez, A., & Li, Z. (2022). Speckle noise reduction for structural vibration measurement with laser Doppler vibrometer on moving platform. *Mechanical Systems and Signal Processing*, *178*, 109196.

Zeng, Y., Núñez, A., & Li, Z. (2023). A simulation study on characterizing transfer functions of railway tracks using train-borne laser Doppler vibrometer. In Maria Pina Limongelli, et al. (eds.), *International conference on experimental vibration analysis for civil engineering structures* (pp. 183–192), Springer Cham, Switzerland.

Zeng, Y., Shen, C., Núñez, A., Dollevoet, R., Zhang, W., & Li, Z. (2023). An interpretable method for operational modal analysis in time-frequency representation and its applications to railway sleepers. *Structural Control and Health Monitoring*, *2023*, 6420772.

Zhai, W. (2020). *Vehicle–track coupled dynamics*. Springer.

Zhang, J., Huang, W., Zhang, W., Li, F., & Du, Y. (2021). Train-induced vibration monitoring of track slab under long-term temperature load using fiber-optic accelerometers. *Sensors*, *21*(3), 787.

How to cite this article: Zeng, Y., Núñez, A., & Li, Z. (2024). Railway sleeper vibration measurement by train-borne laser Doppler vibrometer and its speed-dependent characteristics. *Computer-Aided Civil and Infrastructure Engineering*, 1–19. https://doi.org/10.1111/mice.13150

APPENDIX A: TRAIN-TRACK-LDV MODEL

In the train-track model, the Ritz method is employed to characterize the dynamics of the rail. The modal displacement in the h-th modal coordinate is denoted as $q_h(t)$, and the h-th modal function is defined as follows (Zhai, 2020):

$$Z_h(x) = \sqrt{\frac{2}{m_r l}} \sin \frac{h\pi x}{l} \tag{A.1}$$

where the length of the rail is $l = n_s \times d_s$.

The displacement of the rail is then approximated as the superposition of the first n_m modal displacements as follows.

$$z_r(x,t) = \sum_{h=1}^{n_m} Z_h(x)\, q_h(t) \tag{A.2}$$

Based on the separation of x and t in Equation (A.2), Equation (4) can then be converted into the following second-order ordinary differential equations:

$$\begin{aligned} &\ddot{q}_k(t) + \sum_{i=1}^{n_s} c_{ri} Z_k(x_{si}) \sum_{h=1}^{n_m} Z_h(x_{si})\, \dot{q}_h(t) + \frac{EI}{m_r}\left(\frac{k\pi}{l}\right)^4 q_k(t) \\ &+ \sum_{i=1}^{n_s} k_{ri} Z_k(x_{si}) \sum_{h=1}^{n_m} Z_h(x_{si})\, q_h(t) - \sum_{i=1}^{n_s} k_{ri} z_{si}(t) Z_k(x_{si}) \\ &- \sum_{i=1}^{n_s} c_{ri} \dot{z}_{si}(t) Z_k(x_{si}) = F_c(t) Z_k(x_c(t))\, k = 1, \ldots, n_m \end{aligned} \tag{A.3}$$

The simulation parameters are listed in Table A1.

APPENDIX B: SPECKLE TRANSLATION MODEL

The electric field of the reference beam on the photodetector is described as follows (Martarelli, 2001):

$$E_R = A_R \exp\left[i\left(\frac{2\pi}{\lambda} t + \omega_R t + \theta_R\right)\right] \tag{B.1}$$

where A_R and θ_R represent the amplitude and phase of the reference beam, respectively.

Each speckle has its own amplitude and phase, denoted as A_{Sk} and θ_{Sk} for the k-th speckle. Given the target vibration $z(t)$, the electric field of the k-th speckle is expressed as follows (Martarelli, 2001).

$$E_{Sk} = A_{Sk} \exp\left[i\left(\frac{2\pi}{\lambda} t - 2\frac{2\pi}{\lambda} z(t) + \theta_{Sk}\right)\right] \tag{B.2}$$

Then, each speckle on the photodetector is heterodyned with the reference beam, and the intensity of such a mixed area is derived as follows (Denman et al., 1996):

$$\begin{aligned} I_k(t) &= [E_R + E_{Sk}] \times [E_R + E_{Sk}]^H \\ &= A_R^2 + A_{Sk}^2 + 2A_R A_{Sk} \cos\left(\omega_R t + \frac{4\pi}{\lambda} z(t) + \theta_R - \theta_{Sk}\right) \\ &= I_R + I_{Sk} + 2\sqrt{I_R I_{Sk}} \cos\left(\omega_R t + \frac{4\pi}{\lambda} z(t) + \theta_R - \theta_{Sk}\right) \end{aligned} \tag{B.3}$$

TABLE A1 Parameters for simulating sleeper vibration.

Symbol	Parameter	Value
m_v	Mass of vehicle	50 kg
k_v	Stiffness of suspension	230 kN/m
c_v	Damping of suspension	100 N/(m/s)
m_w	Mass of wheel (including axel box)	40 kg
r_w	Radius of wheel	0.065 m
m_r	Mass of rail per unit length	3.51 kg/m
I	Second area moment of rail	50803 mm^4
n_m	Truncated order of rail modes	25
E	Elastic modulus of rail	205.1 GPa
k_r	Stiffness of rail pad	200 MN/m
c_r	Damping of rail pad	1.9 kN/(m/s)
n_s	Number of sleepers	25
m_s	Mass of sleeper	1.15 kg
d	Sleeper width	0.04 m
d_s	Sleeper spacing	0.1258 m
k_s	Stiffness of sleeper pad	10 MN/m
c_s	Damping of sleeper pad	860 N/(m/s)
P_r	Power of Gaussian white noise for rail irregularity	−120 dBW
λ_{pass}	Passband wavelength of rail irregularity	10 mm
λ_{stop}	Stopband wavelength of rail irregularity	0.4 mm
h_{stop}	Stopband attenuation	55 dB
Δx	Laser-wheel offset	0.063 m
Δt	Integration step size	1×10^{-5} s
γ	Integration parameter	0.5
β	Integration parameter	0.25

where ^{H} denotes conjugate transpose, I_R and I_{Sk} are intensities of the reference beam and the k-th speckle, respectively.

The last term in Equation (B.3) carries the phase change due to the target motion and the laser speckle. After filtering out the first two terms without periodicity and summing up the contributions of all the K speckles, the output of the photodetector is (Denman et al., 1996)

$$u(t) \propto \sum_{k=1}^{K} a_k 2\sqrt{I_R I_{Sk}} \cos\left(\omega_R t + \frac{4\pi}{\lambda} z(t) + \theta_R - \theta_{Sk}\right)$$
$$= 2\sqrt{I_R} I_M \cos\left(\omega_R t + \frac{4\pi}{\lambda} z(t) + \theta_M\right) \quad \text{(B.4)}$$

where θ_M is expressed in Equation (8) and I_M is expressed as follows (Rothberg & Halkon, 2004):

$$I_M = \sqrt{\sum_{p=1}^{K}\sum_{q=1}^{K} a_p a_q \sqrt{I_{Sp} I_{Sq}} \cos\left(\theta_{Sp} - \theta_{Sq}\right)} \quad \text{(B.5)}$$

TABLE B1 Parameters for simulating speckle noise.

Symbol	Parameter	Value
λ	Wavelength of laser	1550 nm
w	Diameter of laser spot	0.19 mm
A	Number of speckles covered by photodetector length	2
R	Distance between target and photodetector	2.7 m
m	Number of grids along the translation direction	200
n	Number of grids along the orthogonal direction	100
f_C	Cut-off frequency of low-pass filter	100 kHz

The target vibration $z(t)$ can be measured from the frequency of $u(t)$, as expressed in Equation (7). The speckle noise is caused by the phase change rate $d\theta_M/dt$, which depends on the properties of the laser speckles. Assuming that the laser is well-focused on the target surface, the space correlation length of the speckles on the photodetector is calculated as follows (Asakura & Takai, 1981):

$$l_C = \frac{\lambda R}{\pi w} \quad \text{(B.6)}$$

where w is the diameter of the laser spot and R is the distance between the target surface and the photodetector. The length l_C describes the size of each speckle, within which the intensity and phase, I_{Sk} and θ_{Sk}, are constant. The intensity and phase of all speckles are assumed to follow the following negative exponential distribution and uniform distribution, respectively (Denman et al., 1996):

$$P(I_S) = \frac{1}{\langle I_S \rangle} \exp\left(-\frac{I_S}{\langle I_S \rangle}\right) \; I_S > 0 \quad \text{(B.7)}$$

$$P(\theta_S) = \frac{1}{2\pi} \; -\pi \le \theta_S \le \pi \quad \text{(B.8)}$$

where $< I_S >$ denotes the mean speckle intensity. Random samples of I_{Sk} and θ_{Sk} are generated for each speckle.

Meanwhile, the time correlation length of the speckles on the photodetector is as follows (Asakura & Takai, 1981):

$$\tau_C = \frac{1}{|v|}\left(\frac{1}{w^2} + \frac{1}{l_C^2}\right)^{-1/2} \quad \text{(B.9)}$$

The simulation parameters are listed in Table B1.